ARMA 23–804

Using Low-Field Nuclear Magnetic Resonance and X-ray Computed Microtomography Imaging to Explore Potential of Microbially-Induced Calcium Carbonate Precipitation Treatment to Seal Shale Fractures

Willett, M.R., Seymour, J.D.
Department of Chemical Engineering, Montana State University, Bozeman, MT, United States
Center for Biofilm Engineering, Montana State University, Bozeman, MT, United States
Bedey, K., Kirkland, C.M., Phillips, A.J. and Cunningham, A.B.
Department of Civil Engineering, Montana State University, Bozeman, MT United States
Center for Biofilm Engineering, Montana State University, Bozeman, MT, United States
Dobeck, L.
Energy Research Institute, Montana State University, Bozeman, MT, United States
Center for Biofilm Engineering, Montana State University, Bozeman, MT, United States
Crandall, D.
National Energy Technology Laboratory, Morgantown, WV, United States
Rutqvist, J.
Lawrence Berkeley National Laboratory, Berkeley, CA, United States

ABSTRACT: Microbially-induced calcium carbonate precipitation (MICP) is a biological process in which microbially produced urease enzymes convert urea and calcium into solid calcium carbonate ($CaCO_3$) deposits. Studies have shown that MICP can be used to seal fractures in shale, raising the possibility of applying this technology to restimulate fracking wells by plugging underperforming fractures. For this and other applications to become a reality, non-invasive tools are needed to determine how effectively MICP seals shale fractures under subsurface conditions. In this study, a 2.54 cm wide and 5.08 cm long Marcellus shale core with a single, ~1 mm wide fracture held open by sand "proppant" underwent MICP-treatment at 60°C until reaching three orders of magnitude permeability reduction. Low-field nuclear magnetic resonance (LF-NMR) and X-Ray computed microtomography (μ-CT) techniques were used to assess the extent of biomineralization within the fracture. These tools revealed that while $CaCO_3$ precipitation occurred throughout the fracture, there was preferential precipitation around proppant, and the core sealed at the effluent end before filling most of the fracture. Both tools were able to independently calculate of the amount of solid biomineral formed inside the fracture. This study found that the distribution of proppant within the shale fracture was an important parameter controlling the degree of biomineralization.

1. INTRODUCTION

1.1. Background

Shale is a fine-grained, sedimentary rock often found adjacent to layers of sandstone and limestone up to thousands of feet below ground surface (bgs). The unique characteristics of this formation have led it to play multiple roles in the ever-changing energy landscape of the 21st century. Possessing relatively high porosity but extremely low permeability, shale has been targeted for geologic carbon sequestration and nuclear waste disposal (Washburn, 2014). Many shale deposits also contain rich quantities of hydrocarbon fuels, which can be extracted from very tight pore spaces with hydraulic fracturing, also known as fracking. All of these applications highlight a need for methods to control permeability to ensure the long-term safety and utility of these reservoirs. For example, there may be a need for a method to plug fractures that arise in shale used for storage purposes to mitigate leakage. There is also motivation to seal fractures created in fracking wells to prevent contamination of aquifers by fracking fluids or potentially restimulate the

well to enhance natural gas recovery (i.e. "frack/re-frack").

One promising solution is to induce calcium carbonate mineralization within shale fractures to seal possible fluid pathways, a process known as microbially-induced calcium carbonate precipitation (MICP). This "biocementation" technology was first used in the early 1990s to consolidate and plug sand columns (De Muynck et al., 2010). Since then, studies have shown that MICP-treatment can strengthen soil and seal cracks in stone/concrete structures (Phillips et al., 2013). The success of MICP-treatment can be attributed to the fact that it is delivered with non-toxic, low viscosity (aqueous) fluids and microbes that can permeate through small apertures. Indeed, its practicality has led to several successful applications in the field, including sealing sandstone fractures and remediating cement wellbores up to thousands of feet bgs (Cuthbert et al., 2013; Phillips et al., 2016; Phillips et al., 2018; Kirkland et al., 2020). Applying this technology to seal shale fractures, however, presents a new challenge to its viability due to severe subsurface conditions, where temperatures can range from 50-90°C and pressures reach 34.5 MPa (Hasan & Reza, 2019).

1.2. MICP

MICP occurs through the degradation of urea, one of the mechanisms involved in the nitrogen cycle (Jain et al., 2021). In the first step, the microbially produced urease enzyme catalyzes the hydrolysis of urea into carbamic acid and ammonia (Eq.1). Additional hydrolysis reactions convert carbamic acid to carbonic acid and ammonia to ammonium and hydroxide (Eq. 2-3). These ions increase the pH of the environment and lead to the formation of bicarbonate and then carbonate (Eq. 4-5). Finally, in the presence of calcium, solid calcium carbonate biomineral is formed (Eq. 6) (Phillips et al., 2013):

$$CO(NH_2)_2 + H_2O \xrightarrow{urease} NH_2COOH + NH_3 \quad (1)$$

$$NH_2COOH + H_2O \rightarrow NH_3 + H_2CO_3 \quad (2)$$

$$2NH_3 + 2H_2O \leftrightarrow 2NH_4^+ + 2OH^- \quad (3)$$

$$H_2CO_3 \leftrightarrow HCO_3^- + H^+ \quad (4)$$

$$HCO_3^- + H^+ + 2OH^- \leftrightarrow CO_3^{2-} + 2H_2O \quad (5)$$

$$Ca^{2+} + CO_3^{2-} \leftrightarrow CaCO_3(s) \quad (6)$$

Only a few studies have explored the effectiveness of MICP-treatment on shale fractures. Cunningham et al. demonstrated that an Opalinus shale core with a single fracture filled with 30/50 sand proppant could be biomineralized under ambient conditions, achieving up to four orders of magnitude permeability reduction (Cunningham et al., 2015). Significantly, one order of magnitude permeability reduction was reached when biomineralizing under high-pressure conditions of 6.12 MPa. Another study showed that MICP-treatment was successful at sealing fractured shale without proppant at elevated temperatures of 60 and 70°C, as determined by a 3-4 orders of magnitude drop in permeability (Hiebert, 2018). Notably in this study, the biomineralized core was pulled apart and breakage occurred in the shale rather than the mineral seal. These results demonstrate that MICP-treatment under subsurface conditions may be feasible, though highlight a need for other, non-invasive tools to determine its effectiveness. Permeability is a bulk measurement and does not reveal any information about the extent of biomineralization within the fracture. Furthermore, taking the fracture apart may destroy important details such as the spatial distribution of $CaCO_3$ precipitation.

1.3. NMR

One non-invasive approach to study the effectiveness of shale biomineralization is nuclear magnetic resonance (NMR). A sample placed in an NMR spectrometer is exposed to a static $\mathbf{B_0}$ magnetic field which causes ^1H nuclei (i.e., protons) within the sample to align their magnetic moments together and form a net magnetization $\mathbf{M_0}$ (Gupta et al., 2021). In a process called "excitation", $\mathbf{M_0}$ is manipulated by additional magnetic fields to create signal. NMR is highly sensitive to water and signal amplitude is directly proportional to the total amount of fluid present in saturated systems. Moreover, in saturated porous media, the rate of signal decay, termed T_2 relaxation, is proportional to the pore surface-to-volume ratio (S/V) (Eq. 7):

$$\frac{1}{T_2} = \frac{1}{T_{2B}} + \rho_2 \frac{S}{V} \quad (7)$$

where T_2 is the overall T_2 relaxation time of the pore in [s], T_{2B} is the T_2 relaxation time of the "bulk" pore fluid in [s], and ρ_2 is the surface relaxivity for T_2 relaxation in [um/s]. Surface relaxivity describes the relaxing strength of the pore wall and is largely influenced paramagnetic compounds found in the sample (Kleinberg et al., 1994). Eq. (7) states that when S/V is very large, as in the case shale nanopores, T_2 relaxation will be dominated by interactions between protons and surfaces and the influence of T_{2B} will be negligible. Conversely, if S/V is very small, T_2 relaxation will be dominated by interactions between the protons themselves and have more bulk fluid relaxation behavior, i.e., longer T_2 relaxation times. Importantly, Eq. (7) is also valid at describing T_2 relaxation within fractures (Golsanami et al., 2016). The large difference between the S/V of large fractures (>>0.2 mm gap) and shale nanopores makes it possible to distinguish the relaxation times of these two hydrogen populations. Thus, from Eq. (7), an NMR T_2 experiment, which measures the distribution of T_2

relaxation times within a sample, can also be used to characterize the distribution of pore sizes and fractures within a porous media. However, NMR signal from shale is complicated because significant amounts of hydrogen can also exist in organic material such as kerogen and bitumen (Washburn, 2014). Fortunately, signal from the various ^{1}H components can be distinguished by exploiting differences in NMR T_1 relaxation times. T_1 relaxation is distinct from T_2 relaxation and describes how protons return to thermal equilibrium following excitation. Motionally restricted components, which include most of the organics in shale, have T_1/T_2>1, while water displays $T_1/T_2 \approx 1$. NMR T_1-T_2 relaxation correlation experiments provide another dimension to separate signal and characterize the various hydrogen populations present inside the sample (Fleury & Romero-Sarmiento, 2016).

Thus, NMR is well-equipped to analyze shale fractures undergoing biomineralization. Tracking how the organic hydrogen, pore water, and fracture water populations change after MICP-treatment can reveal the extent of biomineralization and may also indicate how the organic fraction is affected by MICP. To the author's knowledge, there is no previous work on NMR analysis of biomineralized shale fractures. However, Jin et al. used NMR relaxometry to study freeze-thaw cycles on shale soils consolidated with MICP-treatment (Jin et al., 2020). Increases in T_2 relaxation times and signal were observed in many pores, indicating they were damaged and enlarged by freeze-thaw cycles. Many studies have also used NMR to characterize MICP-treated sandstone. Sandstone is generally more porous has much greater permeability than shale (Washburn, 2014). As expected, NMR revealed that MICP occurs throughout the pore network (Sham et al., 2013; Zhuang et al., 2022). Also relevant is NMR studies of biomineralized sand columns. In shale, fractures can be filled with proppant and microbes are expected to attach to the sand particles as well as the shale. Interestingly, two studies reported that in sand columns undergoing MICP-treatment, water in large pores had longer T_2 relaxation times post-MICP despite an overall reduction in signal (Kirkland et al., 2017; Thrane et al., 2020). However, as $CaCO_3$ fills voids around sand, pore sizes should shrink and result in shorter T_2 relaxation times. It was theorized that this conflicting result was due to mineral formation or gas bubbles generated during precipitation shielding water from paramagnetic impurities of the sand, i.e. reducing the ρ_2. However, another study by Wu et al. reported the opposite trend: enhanced T_2 relaxation along with lower signal from macropore peaks as sand columns were progressively biomineralized (Wu et al., 2017). These findings demonstrate that NMR can produce perplexing results. It is not always apparent whether changes in S/V or ρ_2 will have a greater impact on NMR relaxation. While relaxation times of water in large shale fractures are expected to be similar to those of bulk water, it is possible that the ρ_2 of fracture surfaces may have a small effect. In this case, mineral precipitation on the fracture surfaces may cause T_2 to initially increase before changes in S/V has an impact.

1.4. X-Ray Computed Microtomography (μ-CT)

Despite the versatility of NMR, its characterization of shale is largely limited to bulk measurements. While MRI can spatially localize signal, this is difficult with shale since NMR signal decays rapidly and pushes the limits of conventional signal detection and acquisition (Zamiri et al., 2021). Instead, X-Ray computed microtomography (μ-CT) scanning data, another non-invasive tool, can be used obtain spatially resolved information important for determining the effectiveness of MICP-treatment. CT scanners work by taking multiple X-ray measurements at different angles around a sample (Jung, 2021). X-rays are absorbed or scattered to varying degrees depending on the type of materials they encounter and then transmitted to a detector. 2D cross-sectional images are reconstructed from a series of 1D X-ray projections. 2D images can also be combined to create a 3D image of the object being scanned. Fortunately, characterizing CT signal is much more straightforward than NMR: dark areas in a CT image represent empty spaces and bright regions represent solid materials. Thus, μ-CT can provide a visual of mineral deposition within the fracture as well as quantifiable, spatial measurements of changes in the void fraction due to MICP. Using μ-CT to characterize biomineralization in porous media has been well established (Minto et al., 2017; Tobler et al., 2018; Kirkland et al., 2019).

This study will explore the potential using MICP-treatment to seal a shale core with a single, ~1 mm wide fracture with proppant at 60°C, a temperature reflective of subsurface conditions in shallow shale formations. Two non-invasive tools, LF-NMR and μ-CT, will help explore the extent of biomineralization. Comparisons will be made between the complimentary information provided by each approach as well as a discussion on their unique insights. Ultimately, determining the success of MICP-treatment at the lab scale is a critical step for assessing its feasibility for deployment in the subsurface.

2. MATERIALS AND METHODS

2.1. Materials

Marcellus shale reservoir samples were provided by the National Energy Technology Laboratory (NETL) and sourced from the Yawkey #98 vertical well in Logan Country, West Virginia at a depth of 4,000-4,171.6 ft. A description of the full core can be found in Crandall et al. (Crandall, 2019). 2.54 cm wide cores were drilled perpendicular to the bedding plane and cut into 5.08 cm pieces, then fractured in half lengthwise using a modified

Brazilian test method. To prepare the sample for biomineralization, the fracture surfaces were cleaned and one layer of Granusil 2095 size (10/20) sand (~1 mm in diameter) was spread evenly along one half of a fractured shale core. The other half was placed on top and both pieces were wrapped together with Teflon tape. The estimated volume of the fracture was ~2 mL.

2.2. NMR Measurements

Low-field NMR (LF-NMR) exposes the sample to weaker $\mathbf{B_0}$ magnetic fields compared to "high-field" instruments. This is advantageous for reducing the impact of magnetic field susceptibility artifacts. Shale cores were saturated in brine for 24-48 hours under vacuum prior to NMR analysis. Brine was held inside the fracture during data collection. Instrumentation consisted of a benchtop 2 MHZ Magritek rock core analyzer (RCA) with a 54 mm probe (Magritek, Wellington, New Zealand). T_2 experiments were measured by the Carr-Purcell-Meiboom-Gill (CPMG) pulse sequence. Multi-exponential signal was inverted by the inverse Laplace method to generate a T_2 distribution. T_1-T_2 correlation experiments consisted of an initial inversion recovery sequence followed by a CPMG train. Signal was inverted with the 2-D inverse Laplace method to generate a T_1 versus T_2 distribution. Experiment parameters are listed in Table 1. The inverse Laplace transform was calculated using the non-negative least square (NNLS) fitting function and Tikhonov regularization to minimize the error (Venkataramanan et al., 2002; Callaghan et al., 2003).

Table 1. NMR experimental parameters before and after MICP-treatment.

Parameter	T_2 (Pre/Post)	T_1-T_2 (Pre/Post)
Repetition time (ms)	10000	10000
Echo time (us)	100	100
Number of echoes	30000/40000	30000/40000
Number of scans	128	128
Number of T_1 delays	n/a	32
Min-Max T_1 delay (ms)	n/a	0.1-10000

2.3. μ-CT Scanning

Prior to μ-CT analysis, shale cores were thoroughly dried for 24-48 hours at 60°C and then wrapped in Teflon to prevent proppant from escaping. Instrumentation consisted of a Skyscan 1173 X-ray microtomorgaph (Bruker Corporation, MSU Subzero Science Laboratory). Image resolution was 17.3 μm. To create a complete image of the core, three overlapping sections were scanned every 0.7° for 180°. An exposure of 1200 ms, a voltage of 130 kV, and a current of 60 μA with a brass 0.25 mm filtered beam were used to capture all scans. Prior to each scan a flat field correction was performed to calibrate the initial intensity of the beam. The three overlapping sections of the scans were reconstructed using NRecon software (Bruker Corporation) to produce a series of 2D images, or slices, representing the length of the core. Gaussian kernel smoothing was used during reconstruction to remove noise. Once reconstructed, a circular region of interest (ROI) was drawn around the circumference of the core for each 2D slice using CTAn software (Bruker Corporation). All slices were made binary in CTAn by applying a thresholding to the images to distinguish shale, proppant, and biomineral from void space. Shale, proppant, and mineral represent similar attenuation in a μ-CT scan. The data was sorted into two tonalities: black pixels representing void space within the fracture and white pixels representing proppant and mineral within the fracture and the shale core. Thresholding was applied to all slices of the scan and all slices were made binary to determine how the ROI void space changed along the length of the core. The 2D slices were stacked in CTAn to create a 3D reconstruction of the fractured core. CTAn was used to calculate the area of black pixels in each slice of the scan for quantitative comparison of pre- and post-MICP reconstructions to provide an estimate of mineral formed in the fracture.

2.4. Media

Many bacterial strains produce urease, but *Sporosarcina pasteurii* has been favored for MICP engineering applications due to its high ureolytic activity and biomineral formation rate (Jain et al., 2021). 100 mL of brain heart infusion (37 g/L) amended with urea (20 g/L) was inoculated with 1 mL thawed frozen stock culture of *S. pasteurii* (ATCC 11859). After 24 h., the culture was transferred into yeast extract (YE) media (1% v/v). YE media consisted of 1 g/L ammonium chloride, 15.5 g/L yeast extract, 35 g/L sodium chloride, and 20 g/L urea. After 16 h., the bacteria concentration was assessed by injecting 200 μL of culture into a Greiner Bio-One 96 well flat bottom plate and measuring the optical density (OD) with a Tecan Infinite F50 absorbance reader with a 600 nm filter. OD readings >0.7 were considered high bacteria concentrations and used for injections. Calcium mineralizing media was prepared by combining 20 g/L of urea, 35 g/L sodium chloride, and 1 g/L ammonium chloride; adjusting pH to 6-6.3 with 0.1 M HCl; and then adding 41 g/L calcium chloride dihydrate. Brine consisted of 35 g/L sodium chloride.

2.5. Reactor System

The reactor system consisted of two piston ISCO syringe pumps which separately delivered microbes or calcium mineralizing media to the core holder inside a 60°C oven (Fig. 1). The pump delivering calcium mineralizing media was also equipped with a heated water jacket maintained at 60°C. Pressure was recorded from an Omega Engineering, Inc. PX309 series pressure transducer and Campbell manual pressure gauge. The various components were connected by 1/4-in. OD stainless steel tubing.

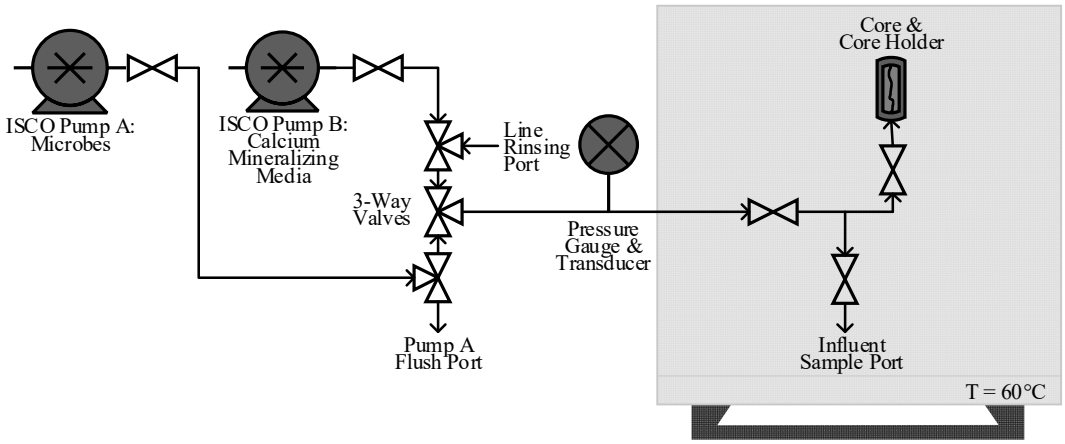

Fig. 1. Schematic of the reactor system. Pump A delivered *S. pasteurii* culture to the core inside a 60°C oven. Following a brief attachment period, pump B delivered pre-heated calcium mineralizing media also at 60°C to the core. This was followed by a resting 2 h. batch period. Pressure drop across the core was measured with a pressure transducer or gauge in order to calculate apparent permeability for each injection.

The core holder was adapted from an approach by Cunningham, et al. and consisted of a 15.24 cm length of 2.54 cm diameter reinforced PVC tubing (Cunningham et al., 2015). The Teflon-wrapped core with proppant was enclosed in heat shrink tubing and then inserted into the PVC tubing. Additional overburden pressure was provided by two heavy duty hose clamps placed around both ends of the core, which were tightened to 3.4-4.5 N-m with a torque-wrench. The core holder was connected to the stainless steel tubing system with a hose adapter fitting and rubber tubing. The maximum pressure of the core holder was estimated to be 207 kPa.

2.6. Injection Strategy

A pulsed flow injection strategy was employed in this study. First, the core was inoculated with *S. pasteurii* culture. For injections 1-17, microbes were injected quickly using a manual syringe connected to the influent sample port, followed by a 15 minutes resting period for bacterial attachment. Next, calcium mineralizing media was pulsed at 5 mL/min until reaching the influent side of the core, then 1 mL/min while flowing through the core. After delivering 1-2 times the volume of the fracture, the valve beneath the core was closed and the reaction was allowed to proceed for a two-hour period. Resting batch periods were concluded with a quick brine flush using a manual syringe. After injection 17, due to an increase in pressure, microbe injections and brine flushes were delivered at 1 mL/min using an ISCO syringe pump. Flow rates of all medias were adjusted/lowered with each subsequent injection to ensure pressure did not exceed system limits. MICP pulsed flow treatments were continued until reaching at least 3-orders of magnitude apparent permeability reduction.

2.7. Apparent Permeability

Flow through a shale fracture filled with proppant can be characterized as flow through a porous media. Thus, Darcy's Law was used to calculate the apparent permeability (Eq. 8):

$$k = \frac{Q \cdot \Delta L \cdot \mu}{A \cdot \Delta P} \tag{8}$$

where k is the apparent hydraulic permeability of the fracture, Q is the volumetric flow rate of the fluid, μ is the viscosity of the fluid, A is the cross-sectional area of the fracture, ΔL is the length of the core/fracture, and ΔP is the pressure drop across the flow path (Zimmerman & Bodvarsson, 1996). The gap of the fracture, which is needed to calculate A, was estimated using the cubic law for fracture flow (Eq. 9):

$$b = \left(\frac{12 \cdot \mu \cdot Q \cdot L}{w \cdot \Delta P}\right)^{1/3} \tag{9}$$

where b is the aperture size of the fracture, Q is the volumetric flow rate, L is the fracture length, w is the aperture width, μ is the dynamic viscosity of the fluid, and ΔP is the pressure drop across the flow path (Zimmerman & Bodvarsson, 1996).

2.8. Experimental Workflow

Fig. 2 illustrates an overview of the measurements and experiments for the rock sample. NMR and post-MICP µ-CT analyses were performed on the core securely wrapped in Teflon tape, though pre-MICP and µ-CT testing was performed while the core was inside the core holder.

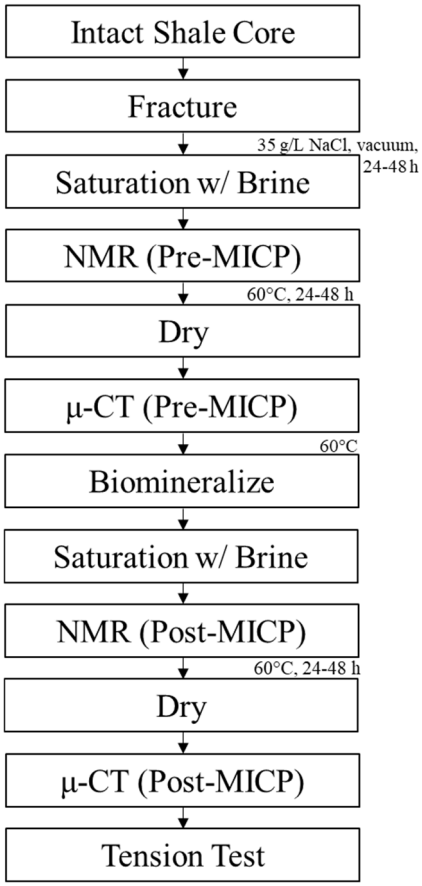

Fig. 2. Schematic of the experimental workflow. Following the non-invasive testing, mechanical properties of the biomineralized shale core will be analyzed with tensile strength testing (Bedey et al., 2023).

3. RESULTS AND DISCUSSION

3.1. Apparent Permeability

The initial apparent permeability was calculated to be 7.0 × 10^5 mD at a flow rate of 20 mL/min through the fracture (Fig. 3). After 26 pulsed flow injections, the apparent permeability was reduced to 9.2× 10^2 mD at a flow rate of 0.03 mL/min, and the core was removed for NMR and μ-CT analysis. Two other cores not presented in this paper also achieved three orders of magnitude apparent permeability reduction under the experimental conditions of this study, confirming that biomineralization at an elevated temperature of 60°C can result in significantly restricted flow. However, photographs of both ends of the cores post-MICP revealed more extensive sealing at the effluent side versus the influent side, indicating precipitation was not uniform (Fig. 4).

3.2. Characterizing NMR Signal from Fractured Shale

Before analyzing NMR results of the biomineralized core, it was important to confirm that signal from a single, large fracture was distinguishable from the various hydrogen

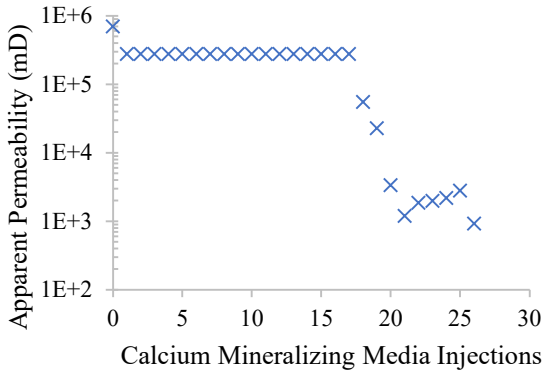

Fig. 3. Apparent permeability as a function of calcium mineralizing media injections. The calculations were done using the pressure and flow measurements taken at the end of each injection cycle, just before the 2-hour resting period started. However, for the initial and final permeability measurements, the flow was continued until pressure reached equilibrium. After the 26th injection, three orders of magnitude permeability reduction was achieved.

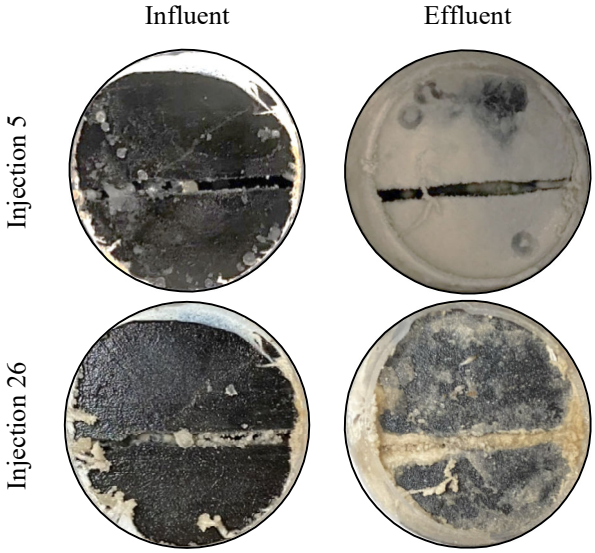

Fig. 4. Photographs of influent/effluent sides of the core after the 5th and 26th batch injection. The effluent side of the core appeared more fully sealed than the influent side after full MICP-treatment.

populations within shale. Fig. 5 shows the T_1-T_2 relaxation correlations for a saturated Marcellus shale core, pre- and post-fracture. The intact core (top) displays dominant signal along the line $10< T_1/T_2<1000$ at T_2~0.1 ms, a regime attributed to bitumen, kerogen, and structural water within the shale (Mukhametdinova et al., 2021). However, due to the echo time limitation, NMR signal that decays before 0.1 ms cannot be fully resolved. Spectral features generated by the inverse Laplace transform before this value are questionable. Shorter echo times or alternative pulse sequences such as the T_1-T_2^* measurement may be able to completely characterize these populations, but the focus of this paper will be analyzing water within shale pores and fractures pre- and

post-MICP with spin-echo experiments (Zamiri et al., 2021). To that end, signal from water within the shale appears along the parity line $T_1/T_2 \sim 1$ and $0.1<T_2<10$ ms. Since clay-bound water signal appears around the limit of detection, this signal can be mostly attributed to water trapped within the so-called shale "micropores" (<100 nm) and "mesopores" (100-1000 nm) (Zhang et al., 2020). Certainly, what is missing from the T_1-T_2 relaxation correlation is equally important as what it reveals. There is no signal from larger shale pores, i.e. "macropores" (>1000 nm), which has a reported signature along the parity line between $10<T_2<1000$ ms. Moreover, free or adsorbed oil, a potentially major organic component expected to appear at $T_1/T_2>10$ and $0.1<T_2<100$ ms, is also absent (Mukhametdinova et al., 2021). This is not unusual as shale rock can have a wide degree of variability. This particular sample appears to come from an unproductive well and possess very tight pore spaces. However, this conveniently enables the use of rapid T_2 experiments for quantitative analysis, since there is no signal from oil overlapping with signal from water along the parity line.

The fractured shale core contains 1 mm sand keeping the gap open. Water is held inside the fracture while NMR experiments are conducted. As expected, new signal from bulk water appears along $1<T_1/T_2<10$ and $10<T_2<10{,}000$ ms in the post-fracture T_1-T_2 correlation map (Fig 5, bottom). This region contains multiple modes along the parity line at T_2= 116 and 1067 ms, which reflects that this environment is a porous media in its own right. Multiple water populations are created by sand particles trapped between each other and the layers of rock. This raises a question of whether T_2 distributions of water within the fracture may overlap with the T_2 distributions of shale pore water. The previously identified shale

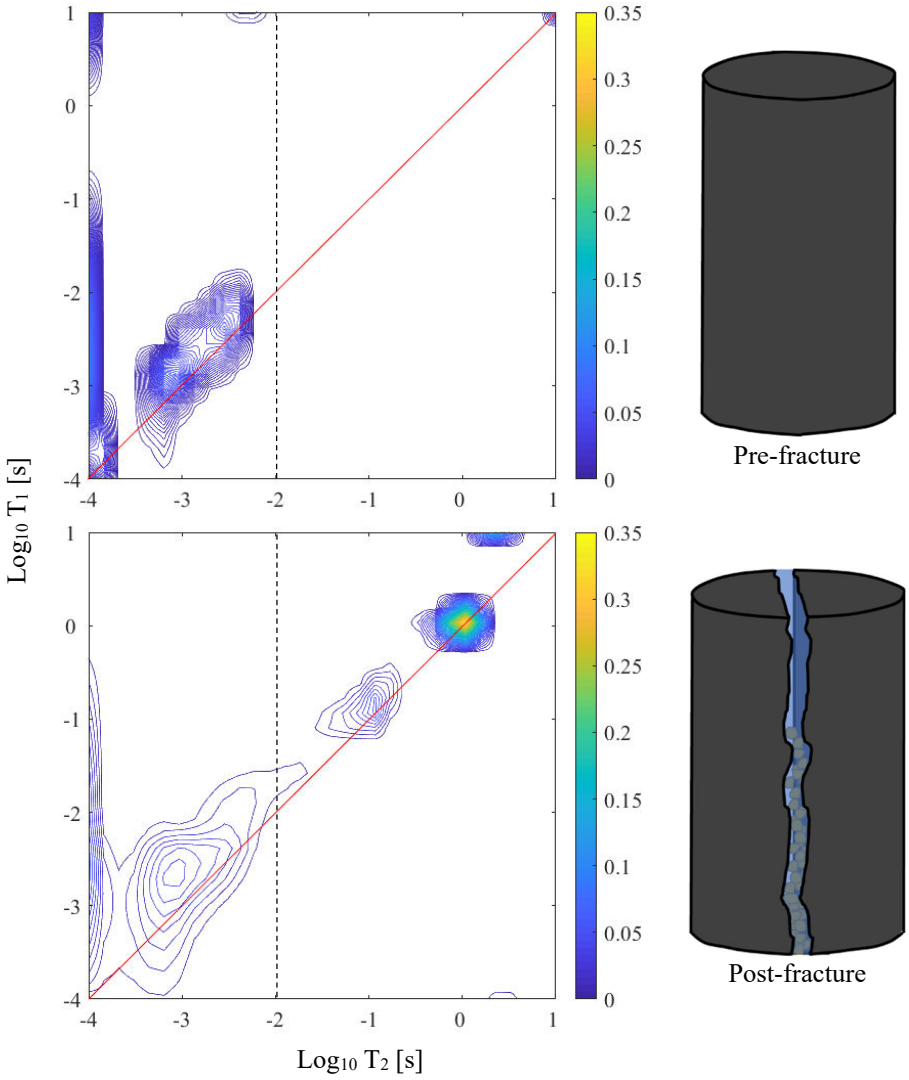

Fig. 5. T_1-T_2 map of a saturated Marcellus shale core before (top) and after (bottom) creating a fluidized fracture with sand proppant. T_1-T_2 correlations can separate the contributions from the different hydrogen populations found within shale. The solid red line is the parity line where $T_1=T_2$ and signal from water is expected to appear. The dashed black line indicates the divide between "fracture water" (to the right) and organics and water from shale nanopores (to the left).

micropore/mesopore range (T_1/T_2~1 and 0.1<T_2<10 ms) appears to extend to 20 ms post-fracture, however the integrated signal intensities are virtually unchanged pre- and post-fracture (<2% drop). This indicates that it is unlikely that signal from the fracture overlaps with signal from the pores. The increase in the range of T_2 times may be a consequence of the 2D ILT finding a slightly different fit due to the large increase in signal post-fracture (+67%). Signal beyond T_2>10 ms can therefore be designated as the "fracture water" zone. It is noteworthy that the most intense signal appears at the T_2=1067 ms mode, which is 17% lower than the T_2 time of pure brine (1292 ms). Most of the bulk water in the fracture behaves like 'free' water, with enhanced relaxation caused by paramagnetic impurities from surfaces.

3.3. Characterizing NMR Signal from Biomineralized Shale Fractures

T_1-T_2 distributions of the Yawkey shale core biomineralized in this study also revealed no signal from free/adsorbed oil, thus T_2 distributions alone are sufficient to characterize biomineralization within the fracture (T_1-T_2 distributions available in Appendix). Fig. 6 shows the T_2 profiles pre- and post-MICP of a Yawkey shale core. Both contain three modes labeled A, B and C from left to right. In the pre-MICP sample, modes B and C are found at 99.6 and 625 ms, respectively, and both possess strong intensities. This implies there are two main populations of bulk water within the fracture. During sample preparation, an even layer of proppant was spread along the length of the core, but after wrapping and setting the core upright for analysis, it was observed that sand particles not tightly pressed between both sides of the core moved down and accumulated at the bottom of the sample. This may have bifurcated the bulk water population into two main groups: restricted water in pore spaces created by proppant at the bottom, represented by peak B, and 'free' water at the top, represented by peak C. The latter has a T_2 time 52% lower than the T_2 time of pure brine, indicating surface relaxation is significant despite the large fracture gap. Peak A is connected to Peak B and exists between the previously identified "pore water" and "fracture water" regions, though mostly the latter. This implies there could be overlap in signal between these two groups, however the gap in signal from 2<T_2<5 ms suggests that water from within this particular core is likely coming from micropores and structural/adsorbed water and that the "fracture water" T_2 distributions are distinct from these populations. It should be noted that during the MICP process, the distribution of proppant in the fracture was expected to change due to hydrodynamic forces caused by injection of fluids.

Post-MICP, peaks A and B shift to lower T_2 relaxation times (-60% and -48%, respectively) with lower intensity

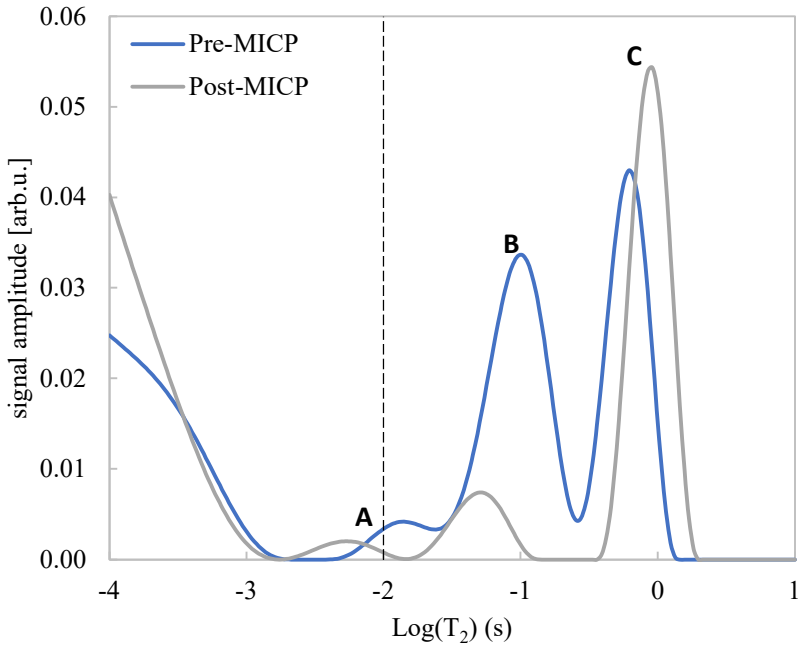

Table 2. T_2 modes from T_2 distributions in Fig. 6

Sample	T_2 Modes (ms)		
	A	B	C
Pre-MICP	13.1	99.6	625
Post-MICP	5.24	52.0	916

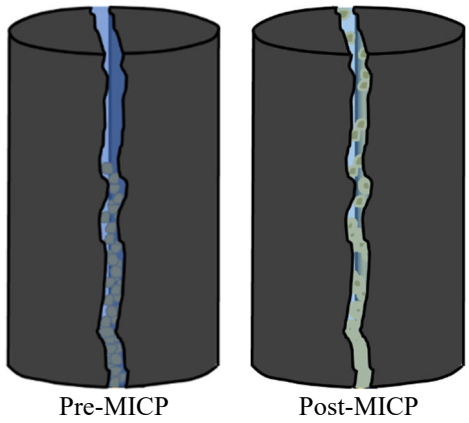

Fig. 6. T_2 distributions for a saturated, fractured Yawkey shale core before (blue) and after (grey) MICP-treatment. The dashed solid line indicates the previously defined "fracture water" zone. Peak C represents 'free' water inside the fracture and peaks A and B represent water bounded within pores created by proppant. Following biomineralization, all of the peaks reduced in intensity and moved to smaller T_2 relaxation times, except peak C. This suggests precipitation formed thoroughly around proppant but significant voids are still present inside the fracture. Note that these illustrations depict how the cores were situated during NMR experimentation. When the core was prepared for pre-MICP NMR analysis, it was observed that some proppant sank to the bottom of the fracture. For post-MICP NMR analysis, the effluent side of the core was flipped to help hold water inside the remaining void regions during data acquisition, since this side of the core appeared to be more thoroughly sealed.

(-52% and -78%, respectively). Since these populations are closely associated with pore spaces created by proppant, the changes suggest that biomineralization is filling these voids. Calcium carbonate formation in a given pore space will displace water, resulting in less signal, and create a smaller pore size, resulting in enhanced T_2 relaxation. Peak C, on the other hand, shifts to a longer T_2 relaxation time and higher intensity (+47%, +26%, respectively) post-MICP. This demonstrates that there is still a significant amount of empty space within the fracture for protons to behave as 'free' water. The increase in T_2 relaxation is indicative of a reduction in surface relaxivity, likely caused by calcium carbonate precipitation on shale surfaces. Thus, the changes in the T_2 distribution suggest biomineralization occurred throughout the fracture, though more thoroughly around regions associated with proppant. This could reflect that microbes more easily attach to proppant instead of shale. Proppant also provides more surface area for microbes to attach and biomineral will likely first bridge both sides of the fracture at these locations. As a result, dense regions of proppant may seal off before precipitation has formed throughout the rest of the fracture. This phenomenon could explain why there is ample signal from 'free' water detected by NMR post-MICP while also observing a significant decrease in apparent permeability.

Unfortunately, hardware constraints obfuscate some potential insight provided by NMR. LF-NMR has lower signal compared to high-field NMR and it is difficult to resolve fast-decaying signal. These limitations make it impossible to track if precipitation is happening within the pores of the shale itself, as with sandstone (Sham et al., 2013; Zhuang et al., 2022). *S. pasteurii* cells have a length of 1.5-10 μm and are too large to diffuse through shale nanopores, though it is theoretically possible for calcium, urea and urease to do so (Wang, 2018). However, the highly permeable fracture undoubtedly presents a preferential flow path for these reactants, in contrast to the extremely low permeability of the shale. Biomineralization should dominate within the fracture and tracking water in this region is well within the capabilities of the NMR tools used in this study.

3.4. μ-CT Scanning Analysis

Fig. 7 displays how the void volume of the fracture quantified by μ-CT varies spatially along the direction of flow through the core, from 0 cm at the influent side to 5 cm at the effluent side. In the pre-MICP data, there is significantly lower void volume (i.e., higher density) at the entrance of the core from approximately 0-0.6 cm. This is likely due to proppant accumulating at the influent side after it was set upright for scanning. Proppant buildup at the entrance of the core can be seen in Fig. 8, the pre-MICP 3D reconstruction of the core. Nevertheless, many pieces are still firmly pressed between the shale halves further up along the core, especially around 4.5-5 cm near the effluent side.

In the NMR results section, it was noted that proppant was expected to redistribute during the biomineralization experiment. This was confirmed by comparing 3D image slices of the core before and after MICP-treatment. The post-MICP scans show that proppant shifted from the influent towards the effluent side of the fracture, resulting in a higher density of proppant at that end. The migration of proppant, coupled with poor biomineral formation at the influent side, likely explains the higher void space (i.e., lower density) observed from 0-0.6 cm post-MICP compared to pre-MICP. However, beyond this point, the void volume is noticeably lower along the length of the core, indicating biomineralization occurred throughout the fracture. Indeed, Fig. 9, the post-MICP 3D reconstruction of the core, reveals $CaCO_3$ precipitation along the surfaces inside the fracture. However, there is more buildup around dense areas of proppant, and it appears the core was plugged at the effluent side. Fig. 7 also shows the largest drop in void volume close to this end, around 4.6 cm. It is notable that despite large voids regions still present through much of the fracture, the seal created near the effluent side was significant enough to achieve three orders of magnitude apparent permeability reduction and prevent further injections.

Preferentially plugging the effluent side of the core is unusual. Typically, the opposite trend is observed, given that the influent side is exposed to reactants first (Phillips et al., 2013). The goal of the pulsed flow injection strategy was to avoid premature influent sealing by injecting reactants quickly and having the transport rate dominate over the reaction rate. Once reactants have reached the effluent side, flow is stopped, and the reaction rate is allowed to dominate and ideally lead to precipitation throughout the fracture. Ultimately, however, biomineral filled spaces around dense areas of proppant first, which happened to be at the effluent side of the core. Distribution of proppant within the fracture appears to be a significant factor controlling the degree of biomineralization.

3.5. Comparing Quantifiable μ-CT and NMR Results

μ-CT is well-suited for calculating the volume of void regions within the fracture before and after MICP-treatment. NMR can provide another approach for calculating these volumes since the integrated area under NMR T_2 distributions is proportional to water volume when the system is saturated. As discussed previously, water signal from the fracture is readily distinguished from shale pore water and organics in these samples. Comparing these measurements of NMR water volume over time can be used to calculate the volume of solid

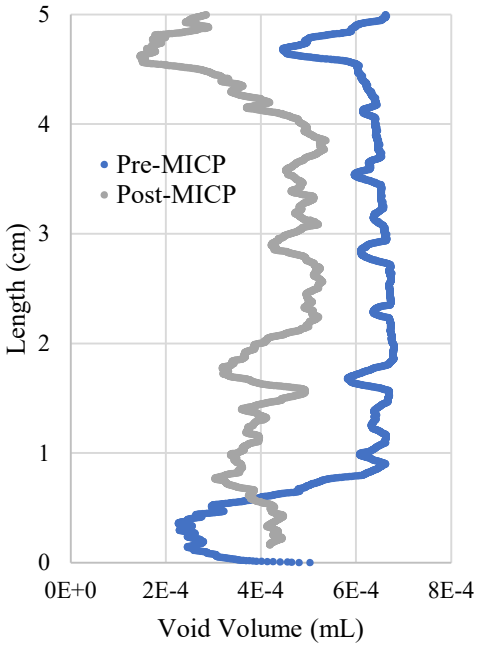

Fig. 7. Void volume calculated by µ-CT along the length of the fracture before (blue) and after (grey) MICP-treatment. Regions further to the left are at a higher density. Post-MICP, there is an overall decrease in the amount of void space present inside the fracture, though the greatest reduction occurs close to the effluent side around 4.6 cm.

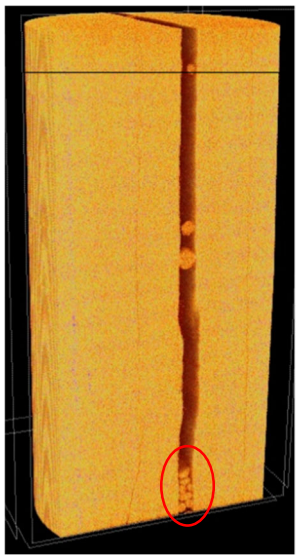

Fig. 8. 3D µ-CT reconstruction, pre-MICP. Proppant accumulated at the bottom of the core during analysis (circled), though other particles are still firmly pressed between both sides of the fracture in other locations.

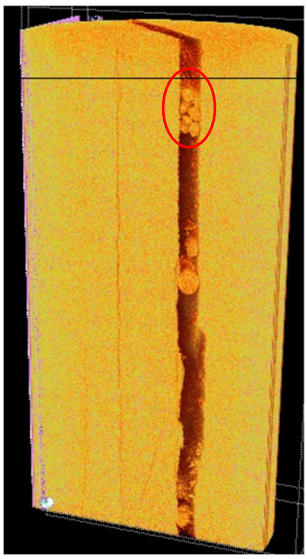

Fig. 9. 3D µ-CT reconstruction, post-MICP. The distribution of proppant inside the fracture switched during the course of the experiment and appeared to accumulate at the effluent side (circled). $CaCO_3$ precipitation can be seen on surfaces inside the fracture, but the most buildup is around proppant and at the effluent side.

biomineral formed inside the fracture. The total volume of calcium carbonate biomineral, $V_{CaCO_3}^{total}$, is composed of its solid and void volume fractions ($V_{CaCO_3}^{solid}$ and $V_{CaCO_3}^{void}$, respectively) (Eq. 10):

$$V_{CaCO_3}^{total} = V_{CaCO_3}^{solid} + V_{CaCO_3}^{void} \quad (10)$$

The initial void volume of the fracture, $V_{pre-MICP}^{void}$, is derived from the saturated, pre-MICP core sample measurement and consists of the difference between the total fracture volume (V_f) and the proppant volume (V_p) (Eq. 11):

$$V_{pre-MICP}^{void} = V_f - V_p \quad (11)$$

The void volume of the fracture post-MICP, $V_{post-MICP}^{void}$, is derived from the saturated, biomineralized core sample measurement and is equal to the difference between the total fracture volume and the volume of solids, which now consist of both proppant and precipitated $CaCO_3$ (Eq. 12):

$$V_{post-MICP}^{void} = V_f - V_p - V_{CaCO_3}^{solid} \quad (12)$$

Thus, the solid biomineral volume, $V_{CaCO_3}^{solid}$, is the difference between the water (void) volumes of the fracture, pre- and post-MICP (Eq. 13):

$$V_{CaCO_3}^{solid} = V_{pre-MICP}^{void} - V_{post-MICP}^{void} \quad (13)$$

The results are summarized in Table 3. Overall, both approaches provide excellent agreement. For practical considerations, pre-MICP µ-CT data was collected while the core was inside PVC tubing, whereas the LF-NMR experiment was performed with the core only wrapped in Teflon. Since the core holder provides considerable overburden pressure, this may have resulted in a smaller initial void volume calculated from the µ-CT data. Post-MICP, there is even stronger agreement because both NMR and µ-CT experiments were run on the biomineralized core after it was removed from the core holder. This study demonstrates that T_2 NMR

Table 3. Calculating volume of solid biomineral using NMR and µ-CT

Volume (mL)	NMR	µ-CT
$V_{pre-MICP}^{void}$	1.78	1.71
$V_{post-MICP}^{void}$	1.15 (-35%)	1.15 (-33%)
$V_{CaCO_3}^{solid}$	0.62	0.56

experiments can provide another approach to complement μ-CT methods for calculating the volume of solid biomineral formed inside fractures.

4. CONCLUSIONS

- MICP-treatment at an elevated temperature of 60°C resulted in a sealed shale core with three orders of magnitude apparent permeability reduction.
- NMR T_1-T_2 maps confirmed distinct T_2 relaxation populations attributed to shale organics, shale pore water, and fracture water.
- NMR T_2 experiments can be used to determine the extent of biomineralization within these shale fractures by analyzing how the peaks shift following MICP-treatment.
- In the post-MICP core, T_2 modes associated with proppant showed reduced signal intensity and relaxation times, while the opposite trend was observed in the T_2 mode associated with 'free' water. This indicated that while precipitation occurred throughout the fracture, it was mainly concentrated around the proppant and noticeable voids were still present inside the fracture.
- μ-CT scanning provides important spatial information and confirmed biomineralization occurred throughout the fracture. Precipitation dominated at the effluent side of the fracture where proppant accumulated.
- NMR and μ-CT data can both be used to calculate the volume of solid biomineral formed inside the fracture.
- Proppant distribution inside the fracture appears to be an important parameter that influences the degree of biomineralization achieved after permeability reduction goals are met. Further experiments are needed with air-gap fractures as well as different proppant distributions and sizes to explore its full effect.

5. ACKNOWLEDGMENTS

The authors would like to thank Evan McCarney for setting up the RCA NMR instrument at the MSU Magnetic Resonance Lab. The authors acknowledge SubZero Science and Engineering Research facility at Montana State University for use of the X-ray μ-CT scanner and data processing and analysis software. This study was supported by funding from the US Department of Energy, Office of Basic Earth Sciences, DOE Award No.: DE-SC0021324. Any opinions, findings, conclusions, or recommendations expressed herein are those of the authors and do not necessarily reflect the views of the Department of Energy (DOE).

REFERENCES

1. Bedey, K., Willett, M. R., Cunningham, A. B., Phillips, A. B., Kirkland, C. M., Dobeck, L., Eldring, J., Crandall, D., & Rutqvist, J. (2023). *Developing Methods to Assess Changes in Mechanical Properties of Shale Modified by Engineered Mineral Precipitation* In preparation for conference proceedings for the 57th US Rock Mechanics/Geomechanics Symposium, Atlanta, GA.
2. Callaghan, P. T., Godefroy, S., & Ryland, B. N. (2003). Diffusion–relaxation correlation in simple pore structures. *Journal of magnetic resonance (1997)*, *162*(2), 320-327. https://doi.org/10.1016/S1090-7807(03)00056-9
3. Crandall, D., Mackey, P., Paronish, T., Brown, S., Moore, J., Workman, S., & Warden, L. . (2019). *Computed Tomography Scanning and Geophysical Measurements of the Rhinestreet and Marcellus Shale from the Yawkey #98 Well* (NETL Technical Report Series, Issue).
4. Cunningham, A. B., Gerlach, R., Phillips, A., Lauchnor, E., Rothman, R., Hiebert, R., Busch, A., Lomans, B. P., & Sprangler, L. (2015). Assessing Potential for Biomineralization Sealing in Fractured Shale at the Mont Terri Underground Research Facility, Switzerland. In *Carbon Dioxide Capture for Storage in Deep Geological Formations* (Vol. 4, pp. 887-903). CPL Press and BP.
5. Cuthbert, M. O., McMillan, L. A., Handley-Sidhu, S., Riley, M. S., Tobler, D. J., & Phoenix, V. R. (2013). A field and modeling study of fractured rock permeability reduction using microbially induced calcite precipitation. *Environ Sci Technol*, *47*(23), 13637-13643. https://doi.org/10.1021/es402601g
6. De Muynck, W., De Belie, N., & Verstraete, W. (2010). Microbial carbonate precipitation in construction materials: A review. *Ecological Engineering*, *36*(2), 118-136. https://doi.org/10.1016/j.ecoleng.2009.02.006
7. Fleury, M., & Romero-Sarmiento, M. (2016). Characterization of shales using T1–T2 NMR maps. *Journal of Petroleum Science and Engineering*, *137*, 55-62. https://doi.org/10.1016/j.petrol.2015.11.006
8. Golsanami, N., Sun, J., & Zhang, Z. (2016). A review on the applications of the nuclear magnetic resonance (NMR) technology for investigating fractures. *Journal of Applied Geophysics*, *133*, 30-38. https://doi.org/10.1016/j.jappgeo.2016.07.026
9. Gupta, A., Stait-Gardner, T., & Price, W. S. (2021). Is It Time to Forgo the Use of the Terms "Spin-Lattice" and "Spin-Spin" Relaxation in NMR and MRI? *J Phys Chem Lett*, *12*(27), 6305-6312. https://doi.org/10.1021/acs.jpclett.1c00945
10. Hasan, M. R., & Reza, M. T. (2019). Hydrothermal deformation of Marcellus shale: Effects of subcritical water temperature and holding time on shale porosity and surface morphology. *Journal of Petroleum Science and Engineering*, *172*, 383-390. https://doi.org/10.1016/j.petrol.2018.09.078
11. Hiebert, D. (2018). *Permeability control for enhanced oil and gas recovery in unconventional reservoirs using advanced mineral precipitation technologies* [Grant]. Butte, MT.
12. Jain, S., Fang, C., & Achal, V. (2021). A critical review on microbial carbonate precipitation via denitrification process in building materials. *Bioengineered*, *12*(1), 7529-7551. https://doi.org/10.1080/21655979.2021.1979862
13. Jin, G., Xu, K., Xu, C., Huang, M., Abdulwahab Qasem, R. G., Guo, S., & Liu, S. (2020). Cementation of Shale Soils by MICP Technology and Its Damage Characteristics Due to Freeze–Thaw Weathering Processes. *Journal of Cold Regions Engineering*, *34*(4). https://doi.org/10.1061/(asce)cr.1943-5495.0000229
14. Jung, H. (2021). Basic Physical Principles and Clinical Applications of Computed Tomography. *Progress in Medical Physics*, *32*(1), 1-17. https://doi.org/10.14316/pmp.2021.32.1.1
15. Kirkland, C. M., Norton, D., Firth, O., Eldring, J., Cunningham, A. B., Gerlach, R., & Phillips, A. J. (2019). Visualizing MICP with X-ray μ-CT to enhance cement defect sealing. *International Journal of Greenhouse Gas Control*, *86*, 93-100. https://doi.org/10.1016/j.ijggc.2019.04.019
16. Kirkland, C. M., Thane, A., Hiebert, R., Hyatt, R., Kirksey, J., Cunningham, A. B., Gerlach, R., Spangler, L., & Phillips, A. J. (2020). Addressing wellbore integrity and thief zone permeability using microbially-induced calcium carbonate precipitation (MICP): A field demonstration. *Journal of Petroleum Science and Engineering*, *190*. https://doi.org/10.1016/j.petrol.2020.107060
17. Kirkland, C. M., Zanetti, S., Grunewald, E., Walsh, D. O., Codd, S. L., & Phillips, A. J. (2017). Detecting Microbially Induced Calcite Precipitation in a Model Well-Bore Using Downhole Low-Field NMR. *Environ Sci Technol*, *51*(3), 1537-1543. https://doi.org/10.1021/acs.est.6b04833
18. Kleinberg, R. L., Kenyon, W. E., & Mitra, P. P. (1994). Mechanism of NMR Relaxation of Fluids in Rock. *Journal of magnetic resonance. Series*

A, *108*(2), 206-214. https://doi.org/10.1006/jmra.1994.1112
19. Minto, J. M., Hingerl, F. F., Benson, S. M., & Lunn, R. J. (2017). X-ray CT and multiphase flow characterization of a 'bio-grouted' sandstone core: The effect of dissolution on seal longevity. *International Journal of Greenhouse Gas Control*, *64*, 152-162. https://doi.org/10.1016/j.ijggc.2017.07.007
20. Mukhametdinova, A., Habina-Skrzyniarz, I., Kazak, A., & Krzyżak, A. (2021). NMR relaxometry interpretation of source rock liquid saturation — A holistic approach. *Marine and Petroleum Geology*, *132*. https://doi.org/10.1016/j.marpetgeo.2021.105165
21. Phillips, A. J., Cunningham, A. B., Gerlach, R., Hiebert, R., Hwang, C., Lomans, B. P., Westrich, J., Mantilla, C., Kirksey, J., Esposito, R., & Spangler, L. (2016). Fracture Sealing with Microbially-Induced Calcium Carbonate Precipitation: A Field Study. *Environ Sci Technol*, *50*(7), 4111-4117. https://doi.org/10.1021/acs.est.5b05559
22. Phillips, A. J., Gerlach, R., Lauchnor, E., Mitchell, A. C., Cunningham, A. B., & Spangler, L. (2013). Engineered applications of ureolytic biomineralization: a review. *Biofouling*, *29*(6), 715-733. https://doi.org/10.1080/08927014.2013.796550
23. Phillips, A. J., Troyer, E., Hiebert, R., Kirkland, C., Gerlach, R., Cunningham, A. B., Spangler, L., Kirksey, J., Rowe, W., & Esposito, R. (2018). Enhancing wellbore cement integrity with microbially induced calcite precipitation (MICP): A field scale demonstration. *Journal of Petroleum Science and Engineering*, *171*, 1141-1148. https://doi.org/10.1016/j.petrol.2018.08.012
24. Sham, E., Mantle, M. D., Mitchell, J., Tobler, D. J., Phoenix, V. R., & Johns, M. L. (2013). Monitoring bacterially induced calcite precipitation in porous media using magnetic resonance imaging and flow measurements. *J Contam Hydrol*, *152*, 35-43. https://doi.org/10.1016/j.jconhyd.2013.06.003
25. Thrane, L. W., Daily, R. L., Thane, A., Kirkland, C. M., McCarney, E. R., Dykstra, R., Codd, S. L., & Phillips, A. J. (2020). Detecting Microbially Induced Calcium Carbonate Precipitation in Porous Systems Using Low-Field Nuclear Magnetic Resonance Relaxometry. *Journal of Geotechnical and Geoenvironmental Engineering*, *146*(4). https://doi.org/10.1061/(asce)gt.1943-5606.0002226
26. Tobler, D. J., Minto, J. M., El Mountassir, G., Lunn, R. J., & Phoenix, V. R. (2018). Microscale Analysis of Fractured Rock Sealed With Microbially Induced CaCO3 Precipitation: Influence on Hydraulic and Mechanical Performance. *Water Resources Research*, *54*(10), 8295-8308. https://doi.org/10.1029/2018wr023032
27. Venkataramanan, L., Yi-Qiao, S., & Hurlimann, M. D. (2002). Solving Fredholm integrals of the first kind with tensor product structure in 2 and 2.5 dimensions. *IEEE transactions on signal processing*, *50*(5), 1017-1026. https://doi.org/10.1109/78.995059
28. Wang, Y. (2018). *Microbial-Induced Calcium Carbonate Precipitation: from Micro to Macro Scale* [Doctor of Philosophy, University of Cambridge].
29. Washburn, K. E. (2014). Relaxation mechanisms and shales. *Concepts in Magnetic Resonance Part A*, *43A*(3), 57-78. https://doi.org/10.1002/cmr.a.21302
30. Wu, J., Wang, X.-B., Wang, H.-F., & Zeng, R. J. (2017). Microbially induced calcium carbonate precipitation driven by ureolysis to enhance oil recovery. *RSC Advances*, *7*(59), 37382-37391. https://doi.org/10.1039/c7ra05748b
31. Zamiri, M. S., MacMillan, B., Marica, F., Guo, J., Romero-Zerón, L., & Balcom, B. J. (2021). Petrophysical and geochemical evaluation of shales using magnetic resonance T1-T2∗ relaxation correlation. *Fuel*, *284*. https://doi.org/10.1016/j.fuel.2020.119014
32. Zhang, P., Lu, S., Li, J., & Chang, X. (2020). 1D and 2D Nuclear magnetic resonance (NMR) relaxation behaviors of protons in clay, kerogen and oil-bearing shale rocks. *Marine and Petroleum Geology*, *114*. https://doi.org/10.1016/j.marpetgeo.2019.104210
33. Zhuang, C., Liu, C., Cui, Z., Yang, Z., Chen, Y., & Dou, Z. (2022). Microbially-Induced Calcium Carbonate Precipitation Test on Yellow Sandstone Based on LF-NMR Monitoring. *Int J Environ Res Public Health*, *19*(24). https://doi.org/10.3390/ijerph192416860
34. Zimmerman, R. W., & Bodvarsson, G. S. (1996). Hydraulic conductivity of rock fractures. *Transport in porous media*, *23*(1), 1-30. https://doi.org/10.1007/BF00145263

APPENDIX

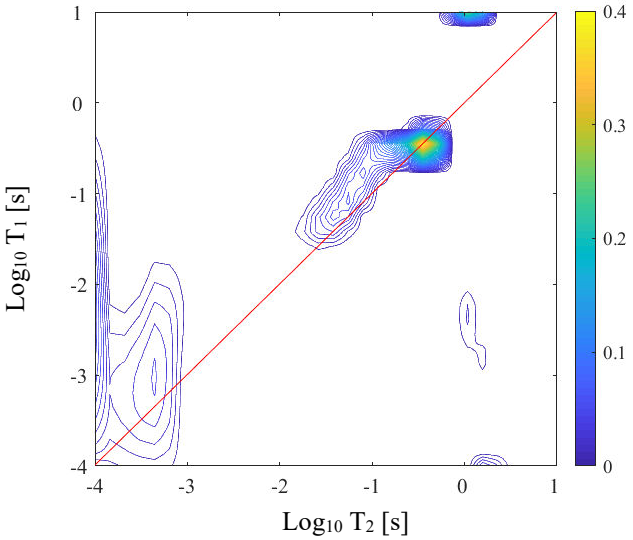

Fig. 10. T_1-T_2 map of a saturated Yawkey shale core, pre-MICP.

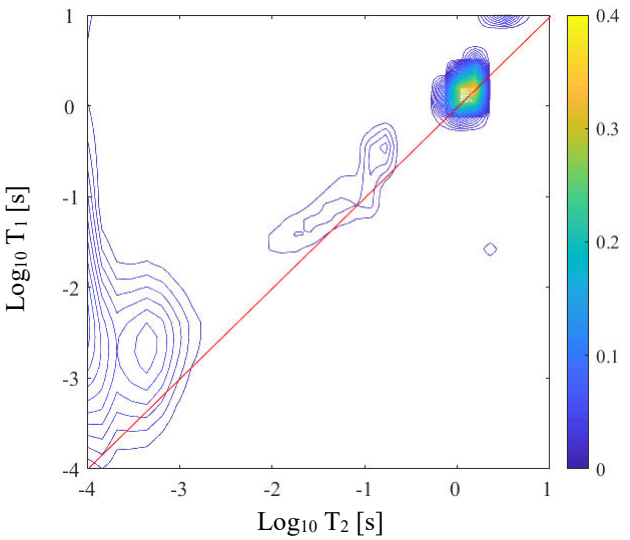

Fig. 11. T_1-T_2 map of a saturated Yawkey shale core, post-MICP.